Article

Relativistic electron acceleration at the bow shock of Jupiter and beyond

https://doi.org/10.1038/s41586-026-10473-z

Received: 28 October 2025

Accepted: 31 March 2026

Published online: 3 June 2026

Open access

Check for updates

Savvas Raptis[1]✉, Drew L. Turner[1], Damiano Caprioli[2], Jamey R. Szalay[3], George Clark[1] & Colby C. Haggerty[4]

Collisionless shocks are ubiquitous in space plasmas throughout the Universe and are widely believed to be primary sites of cosmic ray acceleration[1,2]. The prevailing mechanism, diffusive shock acceleration, requires particles to repeatedly cross the shock front, gaining energy with each crossing. The maximum achievable energy is fundamentally constrained by the Hillas criterion, which relates the physical scale of the accelerator to the maximum particle energy[3]. However, the scarcity of direct observational constraints for acceleration sites limits our ability to predict maximum particle energies across most astrophysical systems. Here, using data from the Juno spacecraft of NASA, we show the direct evidence of relativistic electron acceleration (≥1 MeV) upstream of the bow shock of Jupiter, powered by a large-scale foreshock transient[4,5]. Leveraging these and complementary Solar System observations, we propose a universal scaling law for the Hillas limit that empirically connects the observable size of a transient to maximum particle energy. Applying this scaling to various environments, from planetary bow shocks[6] to protostellar jets[7] and supernova remnants[8], yields a simple model of maximum obtainable particle energies ranging from MeV scales up to about tens of GeV, and about tens of TeV, respectively, providing an observationally grounded method for constraining maximum cosmic ray energies at astrophysical shocks[9,10].

Collisionless shocks are ubiquitous structures in the Universe, widely believed to be the primary sites at which particles are accelerated to relativistic energies, contributing to the cosmic ray population[1–3,11]. The dominant mechanism, diffusive shock acceleration (DSA), describes how particles gain energy by repeatedly crossing a shock front. However, a long-standing challenge, known as the 'injection problem', is that DSA is only efficient for particles that are energetic enough to outrun the shock, a process that depends on the shock inclination and strength, which is not fully understood in all regimes[12–14].

A promising solution lies in the dynamic environment of the foreshock ('precursor' in the astrophysics community)[15,16], which forms upstream of shocks under an oblique or quasi-parallel geometry, where the angle between the shock normal and the ambient magnetic field, $\theta_{Bn} \lesssim 45°$. Within this region, large-scale structures known as foreshock transients can efficiently accelerate low-energy suprathermal particles to relativistic speeds. Recent observations at the bow shock of Earth have demonstrated that these transients can accelerate electrons to about 1 MeV through a powerful synergy of reinforced shock acceleration, pitch angle scattering and geometric trapping[4,5,17–19]. The resulting particle spectra have been shown to be well described by a $E^{-1.5}$ power law attributed to non-relativistic particles undergoing DSA at strong shocks, underscoring the effectiveness of this mechanism and positioning quasi-parallel shocks as exceptional particle accelerators[2,8,13,20,21]. Crucially, these transients (named within the heliophysics community as hot flow anomalies (HFAs), foreshock bubbles and spontaneous HFAs (SHFAs), among others) are fundamental properties of collisionless shocks, forming in diverse plasma environments while scaling with the properties of the host system and its precursor and foreshock[22,23].

The universality of these transient processes is confirmed by observations throughout our Solar System, with foreshock transients identified at Mercury[24], Venus[25], Mars[25–27], Earth[4,5,17–19], Jupiter[28] and Saturn[29]. Studies have shown that the physical scale of these transients correlates directly with the size of the primary planetary bow shock[28]. Applying a principle equivalent to the Hillas limit[3], which connects the size of an accelerator to the maximum particle energy, this scaling suggests a potential link between the global size of a shock system and the maximum particle energy it can produce[5], a hypothesis further supported by kinetic simulations that have consistently reproduced these structures across various parameters[22,30,31].

In this work, we present direct evidence of relativistic (>1 MeV) electrons upstream of the bow shock of Jupiter, conclusively linking their acceleration to a foreshock transient. We demonstrate that the observed energies are consistent with predictions from a scaling law that connects the system size (S) to the acceleration region (L) in foreshock transients and subsequently to an upper energy limit (E_{max}). By validating this scaling with multi-planetary data, we extend our analysis to astrophysical objects, including protostellar jets and supernova remnants. This framework bridges the observational gap between heliophysics and astrophysics through the planetary examples within the Solar System, offering an empirically grounded model for estimating

[1]The Johns Hopkins University Applied Physics Laboratory, Laurel, MD, USA. [2]Department of Astronomy and Astrophysics and E. Fermi Institute, The University of Chicago, Chicago, IL, USA. [3]Department of Astrophysical Sciences, Princeton University, Princeton, NJ, USA. [4]Institute for Astronomy, University of Hawai'i, Honolulu, HI, USA. ✉e-mail: savvas.raptis@jhuapl.edu

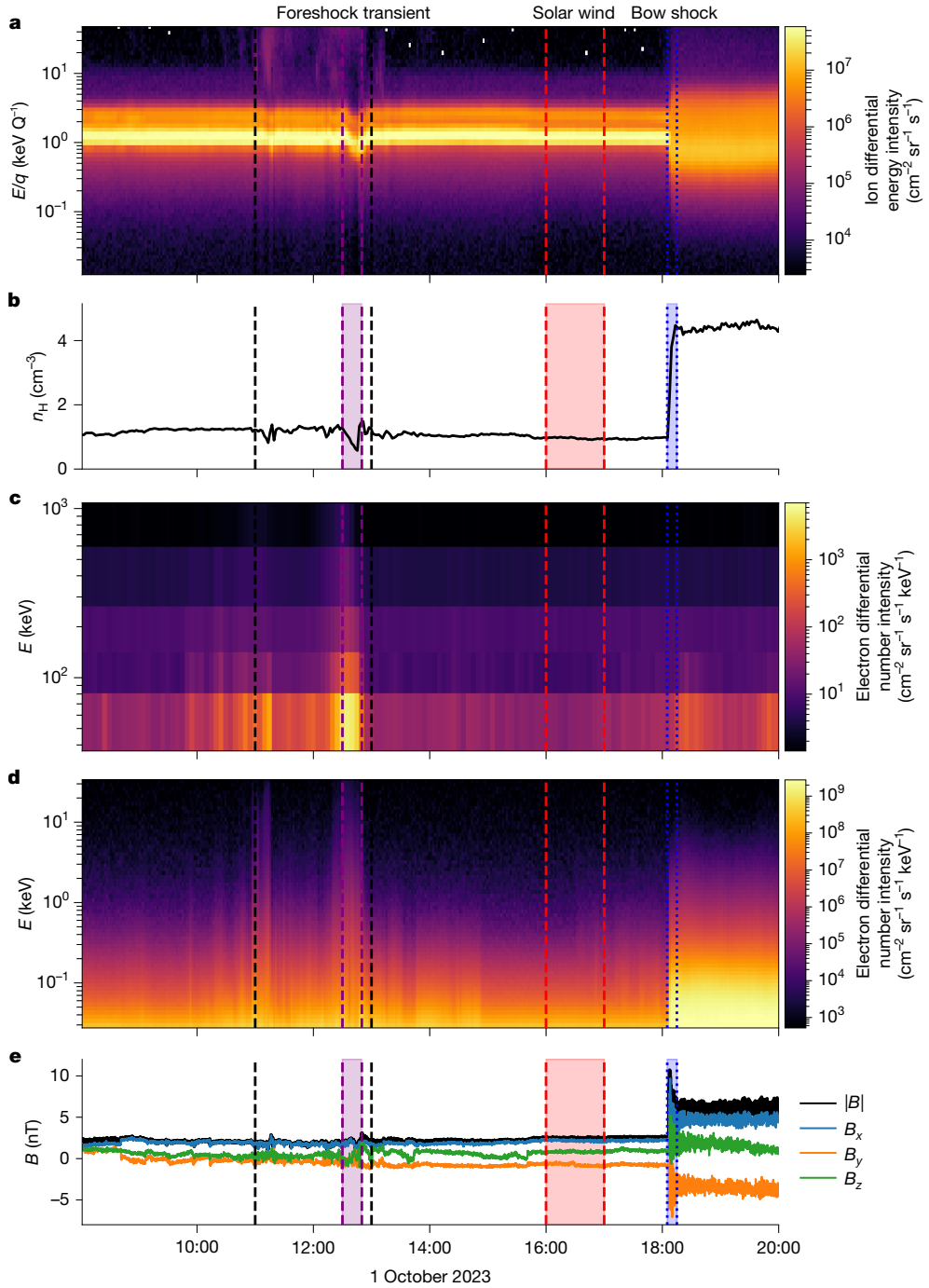

Fig. 1 | In situ observations of the foreshock transient and bow shock crossing at Jupiter. Overview of Juno plasma and magnetic field observations on 1 October 2023 between 08:00 and 20:00 UTC. **a**, Ion energy spectrogram from the JADE instrument. **b**, Proton number density (n_H) derived from JADE (cm^{-3}). **c**, High-energy electron spectrogram from the JEDI instrument. **d**, Low-energy electron spectrogram from JADE. **e**, Magnetic field components and magnitude from the MAG instrument. The interval containing foreshock transients (approximately 11:00–13:00 UTC) is delimited by vertical black dashed lines. The most energetic transient event is highlighted by the purple-shaded region (approximately 12:30–12:50 UTC); this interval corresponds to a strong signal intensity exceeding ambient levels across all energy channels in the high-energy electron spectrum (**c**). For comparison, the planetary bow shock crossing (18:05–18:15 UTC) is indicated by blue-dashed, vertical lines and shading across all panels, and the ambient solar wind conditions are highlighted by the red-shaded area. A detailed view of the transient interval is provided in Extended Data Fig. 1.

the maximum particle energy based on the system size of the shock and its upstream medium. This model can provide key insights into the formation of the cosmic ray spectrum.

Relativistic electrons at the Jovian bow shock

On 1 October 2023, around 18:05 UTC, the Juno spacecraft of NASA[32] was inbound on an orbit at Jupiter, crossing the Jovian bow shock along its duskward flanks. The crossing occurred at approximately [+12.9, +60.5, −59.3] Jupiter radii ($R_J \approx 71,500$ km), in Jupiter Solar Orbital (JSO) coordinates. Before this, Juno probed the Jovian upstream region, obtaining observations from the local solar wind and foreshock environment. An overview of these observations is shown in Fig. 1 between 08:00 and 20:00 UTC. In the interval between approximately 11:00 and 13:00 UTC, the data show a series of localized disturbances associated with

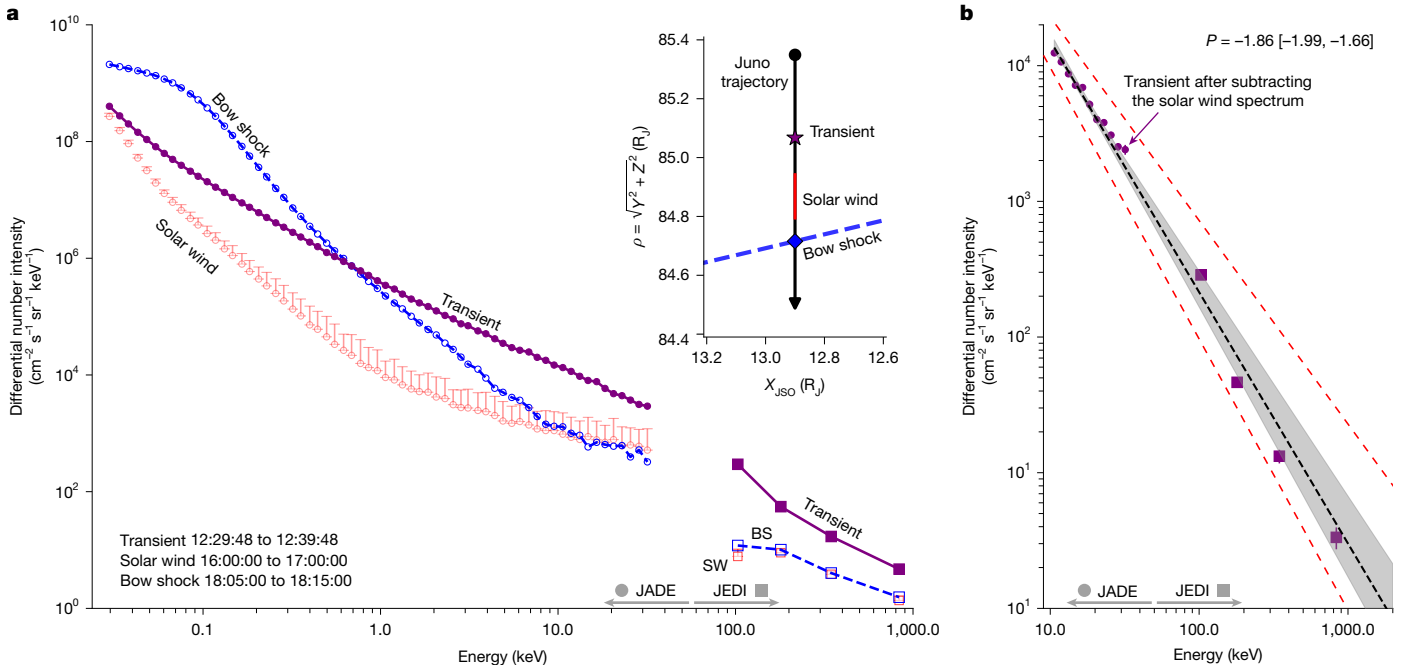

Fig. 2 | Spectral evidence of efficient electron acceleration within the foreshock transient. Combined differential electron number intensity spectra from the Juno spacecraft on 1 October 2023, using observations from the JADE (circles) and JEDI (squares) instruments. **a**, Three distinct plasma environments are compared corresponding to the shaded regions in Fig. 1. The primary foreshock transient event is shown in purple, representing an average over the period of peak intensity. For context, an average spectrum from the nearby bow shock crossing (18:05–18:15 UTC) is shown in blue (dashed lines), and a quiet upstream solar wind interval (16:00–17:00 UTC) is shown in red. The solar wind spectrum (hollow markers) serves as the background level, with upward error bars indicating the 3σ (99%) statistical variability. The two lowest-energy JEDI channels are excluded because of potential contamination. **b**, The solar wind/background-subtracted spectrum for the transient (purple), focusing on the high-energy tail (>10 keV). A fitted power-law index ($\propto E^P$) is shown with its 95% confidence interval determined by bootstrap analysis (Methods). Two reference power laws with spectral indices of $P = -1.5$ and $P = -2.0$, representing theoretical DSA limits for non-relativistic and relativistic particles, respectively, are overlaid (black dashed lines). The inset in **a** shows the trajectory of Juno with respect to the Jovian bow shock in JSO coordinates along with approximate location of each region (Methods).

variations in ion density and the magnetic field, as well as the presence of energetic electrons. This activity appears to consist of two distinct foreshock transient events separated by about 1 h: the first structure being a less developed, smaller-scale transient, whereas the second is a larger event with a more distinct signature across all properties shown in Fig. 1.

Focusing on the more prominent second event, the most intense electron enhancements (Fig. 1c, purple-shaded area) constrain its duration to approximately 12:30–12:50 UTC. Single-spacecraft analysis on this transient (Methods) yields an approximate scale length of $L \approx 3 \times 10^5$ km and an equivalent propagation speed with respect to the planetary shock of $v \approx 320$ km s^{-1}. The characteristics of the transient are as follows: a disruption of the solar wind, evident plasma heating, a localized density decrease and a magnetic field structure with a localized minimum (core) and a compressive edge (Fig. 1a,b,e), clear signatures of a foreshock transient[22]. Its scale corresponds to several Jupiter radii and is consistent with the expectations derived from observations at Earth and other planetary environments[28]. Notably, the peak electron energy during the observed transient is an order of magnitude higher than that observed at the subsequent bow shock crossing (Fig. 1c). This finding supports the view that the most efficient particle acceleration to the highest energies can occur already in the upstream foreshock region, associated with a transient structure, rather than exclusively at the main planetary bow shock front itself. A detailed timeseries plot of the foreshock transient interval is shown in Extended Data Fig. 1, and an illustration of the process is shown in Extended Data Fig. 2.

Figure 2 presents the combined electron energy spectrum from the Juno/Jovian Auroral Distributions Experiment (JADE) (low-energy) and Juno/Jupiter Energetic Particle Detector Instrument (JEDI) (high-energy) instruments during the most intense flux interval, providing a comprehensive overview from the eV range up to 1 MeV. To isolate the accelerated electron population for a direct comparison with theory, we subtract the ambient spectral signal, as shown in Fig. 2b. The energy spectrum from the foreshock transient (Fig. 2 shows a clear signal above the 3σ background level, derived from the red-shaded interval in Fig. 1) across all energy bins for both instruments. Notably, after ambient solar wind background subtraction (Fig. 2b), the energetic part of the electron spectrum is well-bounded by a power law with a spectral index of $P = -1.5$, yet the observed spectrum becomes softer at higher energies, tending towards −2, resulting in a slope of $P \approx -1.85 \pm 0.2$. This is a key result, in agreement with recent findings from foreshock transients at Earth[5,19,33]. Crucially, it demonstrates that this efficient acceleration mechanism can extend to MeV energies around the Jovian bow shock environment. Finally, the spectrum of the adjacent bow shock crossing (Fig. 2, blue line) shows increased intensity up to tens of keV compared to the background solar wind. However, it lacks any acceleration above this energy, suggesting the energetic tail is present only within the foreshock transient observations.

From planetary to astrophysical scales

To generalize our findings, we rely on a key premise that the most efficient particle acceleration in planetary shock environments occurs predominantly within large-scale foreshock transients[4,5,17–19]. In this model, rather than being confined to acceleration strictly normal to the shock front as in classical DSA[1], particles are energized within these transients as the structures themselves propagate along the shock front[22,30]. Crucially, the size of this acceleration region (L) is not an arbitrary local parameter but is intrinsically linked to the global system size, scaling with the standoff distance of the shock (S). This scaling provides the critical physical scale (L) required by the Hillas criterion[3], thereby establishing a direct, empirically constrained relationship

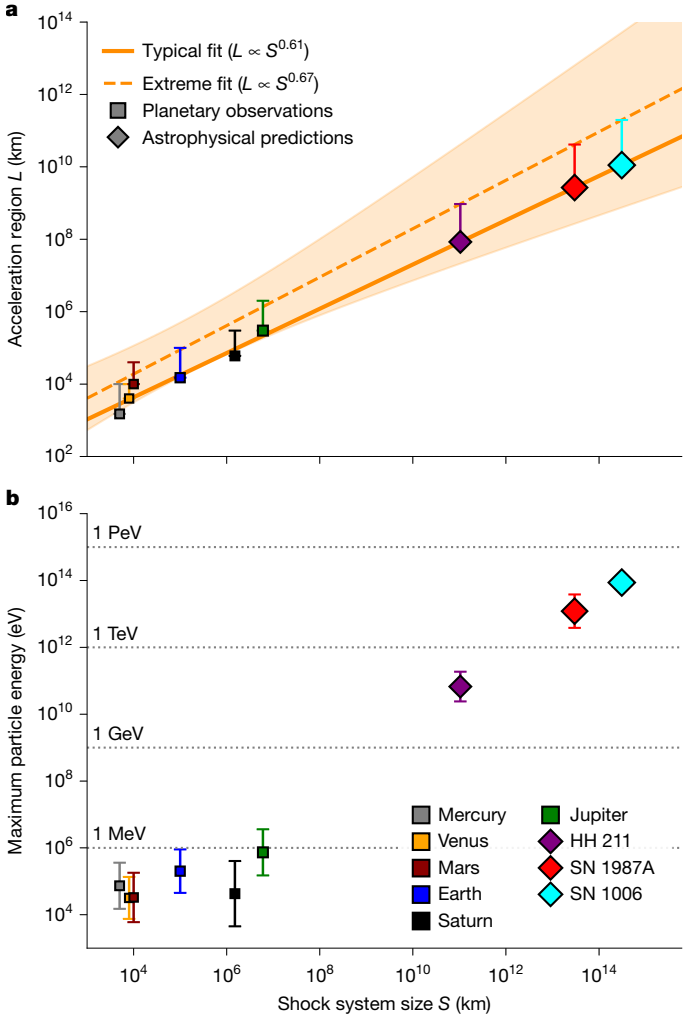

Fig. 3 | Scaling analysis and maximum particle energy for planetary and astrophysical shocks. a, Relationship between shock system scale (S) and the acceleration region size (L). Squares represent observed data for six Solar System planets; solid and dashed orange lines show power-law fits for typical (L_{typ}) and maximum (L_{ext}) observed sizes, respectively. The yellow-shaded area indicates the 95% prediction interval for the extreme fit. For planetary data, upward error bars span from typical to maximum observed sizes. For astrophysical systems (diamonds; HH 211, SN 1987A and SN 1006), markers indicate predicted sizes with error bars extending to the predicted maximum. **b**, Predicted maximum particle energy as a function of S. Planetary energy ranges are calculated from observed maximum L; astrophysical energy ranges are derived from the upper 95% prediction interval of the extreme fit in **a**. Marker sizes scale with maximum predicted energy. Model predictions align with observational evidence: MeV-scale energies at Earth[5,17,18]; Cassini energetic electron events at Saturn[6]; and the MeV Juno measurements at Jupiter reported here. Predicted energies for SN 1006 ($\lesssim$100 TeV) are consistent with X-ray observations[8,38,39].

between the global size of a shock and the maximum particle energy (E_{max}) it can produce. The wealth of in situ observations from our Solar System provides the unique opportunity to empirically determine this relationship, creating a framework that can be generalized to distant astrophysical shocks in which only global parameters can be inferred.

Within this framework, we construct an empirical power-law scaling from planetary in situ observations that connects the global size of a shock (S) to its acceleration region (L) (Fig. 3a). Applying the Hillas limit with this constrained scale (L), along with local shock parameters (Methods), yields maximum particle energies (Fig. 3b) that show remarkable consistency with observations at Earth[5,17,18], Saturn[6] and the new Juno observations at Jupiter presented in this work, demonstrating the applicability of the Hillas limit within the Solar System scales[34]. This successful validation at planetary scales provides the foundation to extrapolate to astrophysical shocks, although we emphasize that this necessarily involves assumptions that extend beyond direct observational constraints. We apply the scaling relationship to the protostellar jet HH 211 and the supernova remnants SN 1987A and SN 1006 systems chosen for their high Alfvén Mach number (M_A) and non-relativistic shocks[7,8,35,36]. Notably, SN 1006 provides an important test of the predictive power of our model, as it is a model for γ-ray bright remnants known to accelerate particles to tens of TeV (ref. 37), enabling a bounded test for the predictions of our model.

Discussion

The presented Juno observations, together with earlier findings at Earth[4,5,18,19], mark a shift in our understanding of particle acceleration at planetary bow shocks. We directly capture relativistic electrons energized not exclusively at the shock front but within its extended shock region, starting at the upstream foreshock, in which a foreshock transient drives electron intensities an order of magnitude above those at the adjacent shock crossing. The immense scale of the transient, spanning several Jupiter radii, and its clean, power-law spectrum to MeV energies confirm that large-scale foreshock transients deliver ideal conditions for efficient acceleration to take place under strong scattering conditions. This insight compels us to revisit the classical DSA picture, expanding it to encompass acceleration along the extended shock region. Building on these results and all available in situ observations from our Solar System, we explored how the intrinsic link between shock geometry and foreshock dynamics governs maximum particle energies across planetary and astrophysical systems.

To generalize beyond Jupiter, we compiled foreshock and shock observations across the Solar System and established a clear scaling between the standoff distance of the shock, S, and the size of its acceleration region, L (Fig. 3a). At Earth ($M_A \sim 4$) and Jupiter ($M_A \sim 20$), foreshock disturbances span scales set by the upstream Mach number[23]. Extending this empirically derived scaling law to protostellar jets (HH 211) and supernova remnants (SN 1987A and SN 1006), which exhibit Mach numbers and global system scales orders of magnitude larger, predicts acceleration regions on the order of 10^8–10^{10} km. Although these scales cannot be directly measured at astrophysical distances, the physical arguments supporting this extrapolation are detailed in the Methods. This approach ultimately proposes a direct link between the global geometry of a collisionless shock and the transient-driven acceleration that sets the maximum particle energy, E_{max}. Using this model, we obtain that for an optimistic but statistically plausible scenario, systems such as SN 1987A could achieve maximum particle energies of the order of $\gtrsim$10 TeV, whereas the predictions for SN 1006 match the maximum energy of $\lesssim$100 TeV inferred from the observations of $\gtrsim$10 TeV γ-rays[8,36,38,39], supporting the presented framework (Fig. 3b).

We must emphasize that this work provides a framework for bridging in situ planetary observations with large-scale astrophysical phenomena. The scaling law of the model, which is the basis for this framework, is derived directly from decades of planetary data. The significance of this approach is underscored by the presented Juno observations, which show that foreshock transients spanning several planetary radii act as highly efficient particle accelerators, which can generate clean power-law spectra up to MeV energies (Fig. 2). Although this observational evidence is strong, the extrapolation to astrophysical shocks necessarily remains tentative (Fig. 3). Consequently, the presented framework represents an attempt to constrain the upper limits of particle acceleration through a unified, observationally driven approach. Furthermore, we should note that our model assumes that Bohm diffusion well describes the environment (that is, the magnetic fluctuations are stronger than the background field, $dB/B_0 \gg 1$) and that sufficient time is available for electrons to get accelerated to the maximum obtainable energies. Consequently, the

derived energy limits should be interpreted as robust, yet relatively conservative bounds. This approach was intentionally chosen for its simplicity, enabling direct predictions from our scaling law and fundamental principles. We acknowledge that more sophisticated models could potentially yield higher or more precise maximum energies. These models can incorporate the complex three-dimensional structure of foreshock transients, which can create distinct scales for particle acceleration and trapping[4,19]. However, these efforts are computationally demanding and necessitate precise a priori knowledge of upstream conditions at a level of detail unavailable for distant astrophysical systems. The precise impact of these complex effects on energy spectra and acceleration timescales remains an open question and constitutes a promising avenue for future investigation.

Conclusions

To summarize, in this work, we present direct evidence of relativistic electrons upstream of the bow shock of Jupiter, associated with a foreshock transient. We demonstrate that these shock-generated transients act as highly efficient particle accelerators, a process previously established at Earth and now shown for the first time at Jupiter. Our observations are in excellent agreement with predictions from shock acceleration operating within the spatial scales dictated by these transients under a strong scattering environment. Using these observations alongside historical data from other planetary environments, we extrapolate this scaling relationship to astrophysical objects, namely, the protostellar jet HH 211 and the supernova remnants SN 1987A and SN 1006. Applying the known parameter space for these non-relativistic shocks shows that these fundamental processes can accelerate particles up to about tens of TeV, an energy range that may contribute to the observed electron cutoff in the cosmic ray spectrum[9]. Most importantly, the predicted maximum energies for SN 1006 are consistent with observations[8,38,39], which provides direct support to our model. Building on this framework, an important next step is to evaluate the presented framework on other astrophysical objects (for example, different supernova remnants, nova shocks[40], ultrahot Jupiters[41] or jets from γ-ray bursts[42]) and determine the relative contributions of various astrophysical accelerators to the cosmic ray flux. These include not only non-relativistic collisionless shocks (as studied here) but also phenomena such as radiation belts[43], massive star clusters[44], blazars[45], ultrafast winds from active galactic nuclei[46] and binary star systems[10]. These endeavours will require extended simulation and observational efforts in a cross-disciplinary manner.

Online content

Any methods, additional references, Nature Portfolio reporting summaries, source data, extended data, supplementary information, acknowledgements, peer review information; details of author contributions and competing interests; and statements of data and code availability are available at https://doi.org/10.1038/s41586-026-10473-z.

1. Blandford, R. D. & Ostriker, J. P. Particle acceleration by astrophysical shocks. *Astrophys. J.* **221**, L29–L32 (1978).
2. Caprioli, D. & Spitkovsky, A. Simulations of ion acceleration at non-relativistic shocks. III. Particle diffusion. *Astrophys. J.* **794**, 47 (2014).
3. Hillas, A. M. The origin of ultra-high-energy cosmic rays. *Annu. Rev. Astron. Astrophys.* **22**, 425–444 (1984).
4. Turner, D. L. et al. Autogenous and efficient acceleration of energetic ions upstream of Earth's bow shock. *Nature* **561**, 206–210 (2018).
5. Raptis, S. et al. Revealing an unexpectedly low electron injection threshold via reinforced shock acceleration. *Nat. Commun.* **16**, 488 (2025).
6. Masters, A. et al. Electron acceleration to relativistic energies at a strong quasi-parallel shock wave. *Nat. Phys.* **9**, 164–167 (2013).
7. Ray, T. P. et al. Outflows from the youngest stars are mostly molecular. *Nature* **622**, 48–52 (2023).
8. Giuffrida, R. et al. The supernova remnant SN 1006 as a galactic particle accelerator. *Nat. Commun.* **13**, 5098 (2022).
9. Aharonian, F. et al. High-statistics measurement of the cosmic-ray electron spectrum with H.E.S.S. *Phys. Rev. Lett.* **133**, 221001 (2024).
10. H.E.S.S. Collaboration Acceleration and transport of relativistic electrons in the jets of the microquasar SS 433. *Science* **383**, 402–406 (2024).
11. Stasiewicz, K. Reinterpretation of Fermi acceleration of cosmic rays in terms of ballistic surfing acceleration in supernova shocks. *Physics* **7**, 51 (2025).
12. Zank, G. P., Rice, W. K. M., Le Roux, J. A., Cairns, I. H. & Webb, G. M. The "injection problem" for quasiparallel shocks. *Phys. Plasmas* **8**, 4560–4576 (2001).
13. Park, J., Caprioli, D. & Spitkovsky, A. Simultaneous acceleration of protons and electrons at nonrelativistic quasiparallel collisionless shocks. *Phys. Rev. Lett.* **114**, 085003 (2015).
14. Gupta, S., Caprioli, D. & Spitkovsky, A. Speed-dependent threshold for electron injection into diffusive shock acceleration. *Astrophys. J. Lett.* **994**, L34 (2025).
15. Drury, L. O. An introduction to the theory of diffusive shock acceleration of energetic particles in tenuous plasmas. *Rep. Prog. Phys.* **46**, 973–1027 (1983).
16. Turc, L. et al. Transmission of foreshock waves through Earth's bow shock. *Nat. Phys.* **19**, 78–86 (2023).
17. Wilson, L. B. III et al. Relativistic electrons produced by foreshock disturbances observed upstream of Earth's bow shock. *Phys. Rev. Lett.* **117**, 215101 (2016).
18. Liu, T. Z., Angelopoulos, V. & Lu, S. Relativistic electrons generated at Earth's quasi-parallel bow shock. *Sci. Adv.* **5**, eaaw1368 (2019).
19. Shi, X., Artemyev, A., Angelopoulos, V., Liu, T. & Wilson, L. B. III Compound electron acceleration at planetary foreshocks. *Nat. Commun.* **16**, 77 (2025).
20. Lalti, A. et al. A database of MMS bow shock crossings compiled using machine learning. *J. Geophys. Res. Space Phys.* **127**, e2022JA030454 (2022).
21. Jebaraj, I. C. et al. Direct measurements of synchrotron-emitting electrons at near-Sun shocks. *Astrophys. J. Lett.* **976**, L7 (2024).
22. Zhang, H. et al. Dayside transient phenomena and their impact on the magnetosphere and ionosphere. *Space Sci. Rev.* **218**, 40 (2022).
23. Burkholder, B. L. et al. Mach number scaling of foreshock magnetic fluctuations at quasi-parallel bow shocks and their role in magnetospheric driving throughout the solar system. *Astrophys. J.* **980**, 7 (2025).
24. Collinson, G. A. et al. Hot flow anomalies at Venus. *J. Geophys. Res.* **177**, A04204 (2012).
25. Collinson, G. A. et al. A survey of hot flow anomalies at Venus. *J. Geophys. Res. Space Phys.* **119**, 978–991 (2014).
26. Collinson, G. et al. A hot flow anomaly at Mars. *Geophys. Res. Lett.* **42**, 9121–9127 (2015).
27. Shestakov, A. Y. & Shuvalov, S. D. Planetary ions acceleration in a hot flow anomaly at Mars. *Planet. Space Sci.* **237**, 105781 (2023).
28. Valek, P. W. et al. Hot flow anomaly observed at Jupiter's bow shock. *Geophys. Res. Lett.* **44**, 8107–8112 (2017).
29. Masters, A. Hot flow anomalies at Saturn's bow shock. *J. Geophys. Res.* **114**, A08217 (2009).
30. Omidi, N. & Sibeck, D. G. Formation of hot flow anomalies and solitary shocks. *J. Geophys. Res.* **112**, A01203 (2007).
31. An, X., Liu, T. Z., Bortnik, J., Osmane, A. & Angelopoulos, V. Formation of foreshock transients and associated secondary shocks. *Astrophys. J.* **901**, 73 (2020).
32. Bolton, S. J. et al. The Juno mission. *Space Sci. Rev.* **213**, 5–37 (2017).
33. Raptis, S. et al. Multimission observations of relativistic electrons and high-speed jets linked to shock-generated transients. *Astrophys. J. Lett.* **981**, L10 (2025).
34. Oka, M., Makishima, K. & Terasawa, T. Maximum energy of particles in plasmas. *Astrophys. J.* **979**, 161 (2025).
35. Araudo, A. T., Padovani, M. & Marcowith, A. Particle acceleration and magnetic field amplification in massive young stellar object jets. *Mon. Not. R. Astron. Soc.* **504**, 2405–2419 (2021).
36. Lemoine-Goumard, M., Acero, F., Ballet, J. & Miceli, M. Hadronic particle acceleration in the supernova remnant SN 1006 as traced by *Fermi*-LAT observations. *Astron. Astrophys.* **693**, A193 (2025).
37. Caprioli, D. Understanding hadronic gamma-ray emission from supernova remnants. *J. Cosmol. Astropart. Phys.* **5**, 26 (2011).
38. Koyama, K. et al. Evidence for shock acceleration of high-energy electrons in the supernova remnant SN1006. *Nature* **378**, 255–258 (1995).
39. Cristofari, P., Blasi, P. & Caprioli, D. Cosmic ray protons and electrons from supernova remnants. *Astron. Astrophys.* **650**, A62 (2021).
40. Diesing, R. et al. Evidence for multiple shocks from the γ-ray emission of RS Ophiuchi. *Astrophys. J.* **947**, 70 (2023).
41. Cauley, P. W., Shkolnik, E. L., Llama, J. & Lanza, A. F. Magnetic field strengths of hot Jupiters from signals of star–planet interactions. *Nat. Astron.* **3**, 1128–1134 (2019).
42. LHAASO Collaboration. A tera-electron volt afterglow from a narrow jet in an extremely bright gamma-ray burst. *Science* **380**, 1390–1396 (2023).
43. Turner, D. L. et al. Universal energy limits of radiation belts in planetary and brown dwarf magnetospheric systems. *Sci. Adv.* **12**, eaea4945 (2026).
44. Aharonian, F. et al. Very-high-energy γ-ray emission from young massive star clusters in the Large Magellanic Cloud. *Astrophys. J. Lett.* **970**, L21 (2024).
45. Liodakis, I. et al. Polarized blazar X-rays imply particle acceleration in shocks. *Nature* **611**, 677–681 (2022).
46. Ajello, M. et al. Gamma rays from fast black-hole winds. *Astrophys. J.* **921**, 144 (2021).

Methods

Data

Observations for this study are from the Juno spacecraft of NASA[32]. The energetic particle data are provided by the JEDI[47], which measures ions and electrons from about 30 keV to 1 MeV with an energy resolution of around 20%. JEDI consists of three identical sensor heads (JEDI90, JEDI180 and JEDI270) distributed around the spacecraft to optimize pitch angle coverage over a 160° × 12° field of view with an angular resolution of about 18°. The first two energy bins of JEDI used in this study are contaminated and are not included in the analysis, resulting in four energy bins covering approximately 100 keV to 1 MeV, as shown in Fig. 2. Lower-energy ion and electron observations are obtained from the JADE[48]. JADE consists of two electron sensors (JADE-E) and an ion sensor (JADE-I), both measuring ions with energy per charge from 10 eV q^{-1} to 46.5 keV q^{-1} across 64 energy channels and electrons with energy per charge from 30 eV q^{-1} to 32 keV q^{-1}, with a time resolution that is mode dependent and corresponds to about 2 min in the presented event. Magnetic field vector data are sourced from the Magnetic Field Investigation (MAG) instrument[49], which uses two fluxgate magnetometers to provide measurements with a temporal resolution of 1 s. All data are presented in the JSO coordinate system, a Jupiter-centred frame in which the x-axis points to the Sun, the y-axis is in the anti-direction of the orbital motion of Jupiter and the z-axis completes the right-handed system[50].

Data post-processing and density calculations

The raw instrument data were processed to generate the products used in this analysis. The JEDI energy-time spectrograms (Fig. 1c) were created by averaging data from all three sensors and all look directions. During the observation period, the instrument operated in a low-resolution mode, binning counts into six logarithmically spaced energy channels from about 30 keV to 1 MeV and into 300 s time bins. The count rates associated with the transient event, ranging from about 20 to 60 counts per second, are considered statistically significant. The electron energy efficiency correction detailed in ref. 51 was applied, although its effect is minimal in the low-radiation environment near the magnetospheric boundary of Jupiter. For JADE, proton densities were derived from JADE-I data using a numerical integration method on SPECIES=3 data[52]. Although JADE-I is not optimized for solar wind measurements[53], this method has been shown to be consistent with forward-modelled Maxwellian fits for similar events[28]. The omnidirectional differential number intensities for JADE-E were calculated by averaging the observed intensities over 48 look directions, which are binned onboard in the low rate science mode of the instrument[48].

Bow shock and foreshock transient characterization

In Extended Data Fig. 1, a magnified timeseries of the foreshock transient interval (11:30–13:30 UTC) is shown. Energetic particle intensification and plasma density depletion begin at about 12:30 UTC, with a localized compression marking the trailing edge of the structure at approximately 12:50 UTC, typical features of foreshock transients[4,5,22,54,55].

To better characterize the global environment during this encounter, we use the local magnetic field conditions and the shock normal vector estimated in ref. 56. Using this, we obtain a normal vector of [0.77, 0.45, −0.44], consistent with the duskward Juno location. The orientation of the magnetic field with respect to this normal is shown in Extended Data Fig. 1e, suggesting that the shock orientation transitions from an oblique or quasi-parallel to a quasi-perpendicular one. Specifically, during the formation and observation of the transient itself, the orientation becomes even more quasi-parallel. This shock geometry (with $\theta_{Bn} \lesssim 60°$) is expected to produce substantial populations of foreshock suprathermal particles[57–59] associated with the formation of foreshock transients[4,5,22,54].

Particle data further support this interpretation. The presence of diffuse, isotropic suprathermal ions and electrons indicates that the spacecraft is residing within the foreshock region[60]. Specifically, the pitch angle distributions (PADs) of ions and especially electrons show a clear isotropic population of accelerated particles. These PADs demonstrate that particles are distributed across all pitch angles, a signature of well-scattered populations within the foreshock. This is in agreement with characteristics of accelerated electrons observed during foreshock transients at Earth[5,18,19]. An illustration of the environment and associated transient is shown in Extended Data Fig. 2.

Focusing on the foreshock transient (12:30–12:50 UT), the electron PAD signature shows a progression as the transient passes through the spacecraft. This signature suggests that particles are accelerated in the approaching region, peaking within the transient and ceasing as the spacecraft exits the structure and the field rotates to a quasi-perpendicular regime after 12:50 UT. This strongly supports a local acceleration mechanism because if the source was external, energetic electrons would be observable over wider intervals. Instead, their strict localization to the transient structure implies they are generated in situ rather than being remote-sensed. Regarding the broader spatial context, based on spacecraft speed (about 4 km s^{-1}) and the interval duration, we estimate that Juno was residing approximately 1R_J upstream of the bow shock (Fig. 2, inset). This serves as an approximate estimate, as the bow shock at planetary flanks can change location rapidly. This estimate is consistent with observations at Earth, in which transients are observed at around 1–4R_E (refs. 19,61,62).

To determine the exact geometry and scale of the observed foreshock transient, we first established its orientation using minimum variance analysis (MVA) on the magnetic field vector data in the JSO coordinate system[63]. This technique identifies the principal axes of the variance of the magnetic field by finding the eigenvalues ($\lambda_{max} \geq \lambda_{int} \geq \lambda_{min}$) and the corresponding eigenvectors of the covariance matrix of the magnetic field over the interval containing the transient crossing. The eigenvector associated with the minimum eigenvalue ($\mathbf{n}_{MVA}$) is interpreted as the normal direction to the boundary of the transient, assuming a quasi-planar structure. The validity of this normal was confirmed by ensuring a large ratio of the intermediate to minimum eigenvalues ($\lambda_{int}/\lambda_{min} \gg 1$). With the boundary normal established, we then estimated the scale size of the transient, L, along this direction using the single-spacecraft timing method. The scale is calculated as $L = |\mathbf{v}_{sw} \cdot \mathbf{n}_{MVA}| \times \Delta t$, where $\mathbf{v}_{sw}$ is the upstream solar wind velocity and Δt is the measured duration of the passage of the spacecraft through the structure. Finally, the convection electric field $-\mathbf{V} \times \mathbf{B}$ points towards the transient sheet, which allows particles to concentrate and form the observed transient. The overall methodological approach we followed is a standardized process typically done when single spacecraft in situ observations are available[4,5,18,28]. Specifically, for our case, we used a typical upstream solar wind velocity of $\mathbf{v}_{sw}$ = [400, 0, 0] km s^{-1} in JSO coordinates, which is in agreement with estimations of velocity during that interval, and calculated the scale as $L = |\mathbf{v}_{sw} \cdot \mathbf{n}_{MVA}| \times \Delta t$, where Δt was taken as a 15-min duration of the passage of the spacecraft during the transient event. It should be noted that this 15-min interval, while relatively conservative, provides a realistic range of values for the spatial scale analysis (described below). The outcome of this analysis is provided in Extended Data Table 1.

Finally, a power-law fitted to the energetic tail of the JADE and JEDI data (≥10 keV) during the foreshock transient results (Fig. 2b) in a spectral index of $P \approx -1.85 \pm 0.2$ with the exact 95% confidence interval being determined using a non-parametric bootstrap analysis with 1,000 iterations[64]. This value suggests an acceleration process with a signature and efficiency similar to that of DSA. The obtained index is well-bounded by the canonical DSA limit of $P = -1.5$, a feature of efficient acceleration, and is also consistent with the expected spectral softening from −1.5 (non-relativistic) towards −2 for electrons at relativistic energies at ≥1 MeV, as they are above the electron rest mass energy[65].

Spatial scales and energy limits

The maximum energy attainable by a charged particle is fundamentally constrained by the physical properties of the accelerating environment. This limit is known as the Hillas criterion[3], which relates the maximum particle energy to the available potential drop across the system. For a characteristic magnetic field B and flow velocity V, the induced motional electric field creates a potential difference across a scale L that ultimately limits the maximum attainable energy of a particle, with charge q, to $E_{max} = qBLV$.

In the specific context of diffusive shock acceleration, this limit can be expressed as a confinement condition requiring that the upstream diffusion length of the particle, L_d, remains comparable to or smaller than the system size L (ref. 34). The diffusion length (L_d) can be estimated through the expression $L_d \approx D/V_{sh}$, where D is the spatial diffusion coefficient for the maximum energy, and V_{sh} is the velocity of the shock. For strong scattering, as is often assumed in the foreshock regions of planetary bow shocks[2,5], the scattering approaches the Bohm limit, at which the diffusion coefficient is $D \approx \frac{1}{3} v r_g$, with v being the relativistic velocity of the particle and r_g its gyroradius. By equating the diffusion length to the system size ($L \approx L_d$), we recover the velocity dependence inherent in the Hillas criterion: $L \approx \frac{1}{3}\frac{v}{V_{sh}} r_g$.

To derive a quantitative expression for the maximum energy from this relationship, we express the velocity v of the particle and gyroradius $r_g = p/(qB)$ in terms of its total energy $E_{total} = E_{max} + mc^2$, where p is the momentum of the particle, q is the particle charge and B is the magnetic field magnitude. The relativistic relations $p = \gamma m v$ and $E_{total}^2 = (pc)^2 + (mc^2)^2$ imply $p = \sqrt{E_{total}^2 - (mc^2)^2}/c$ and $v = pc^2/E_{total}$. Substituting these into the confinement condition gives

$$L = \frac{1}{3}\frac{1}{V_{sh}}\frac{E_{total}^2 - (mc^2)^2}{E_{total}\, qB}, \tag{1}$$

which leads to the quadratic equation for the particle's total energy,

$$E_{total}^2 - (3qBLV_{sh})E_{total} - (mc^2)^2 = 0. \tag{2}$$

Solving this equation for the positive energy root provides the exact solution for the maximum total energy that a size-limited shock acceleration region can produce:

$$E_{max,\,total} = \frac{1}{2}\left[A + \sqrt{A^2 + 4(mc^2)^2}\right], \tag{3}$$

where the term $A = 3qBLV_{sh}$ describes the properties of the accelerator. The maximum kinetic energy is then found by subtracting the rest mass energy of the particle, $E_{max} = E_{max,total} - mc^2$. In the ultrarelativistic limit ($v \to c$ and $E_{total} \gg mc^2$), this relation reduces to the simple linear form $E_{max} \simeq \alpha L$, with $\alpha \simeq 3qBV_{sh}$.

The calculation of energy limits in equation (3) requires three parameters: the local upstream magnetic field strength (B), the shock velocity (V_{sh}) and the characteristic system size (L). In this study, we use the upstream magnetic field for B and the relative velocity between the transient and the primary shock for V_{sh}. The acceleration region size (L) is described by the spatial extent of the transient, which is adequately equated to the precursor or foreshock region.

To model the relationship between the acceleration region size (L) and the characteristic system size (S) as shown in Fig. 3, we assumed a power-law dependency of the form $L = k \cdot S^m$ (ref. 28). Two separate power-law models based on planetary observations are developed: a 'typical' model and an 'extreme' model. For the typical model, we used the standoff distance of each planet as the system size (S) and its typical observed acceleration region size as the associated value for L_{typ}. For the extreme model, we used the same standoff distances (S) but paired them with the maximum observed acceleration region sizes (L_{ext}). We performed a linear fit for each model in the log–log space using ordinary least squares as implemented by the statsmodels (v.0.14.4) of Python library. The resulting fits are shown in Fig. 3a.

The extension from planetary to astrophysical scales follows three points of reasoning: (1) We establish empirically that the acceleration region size (L) scales systematically with the global shock size (S) across planetary environments, where in situ observations confirm that large-scale foreshock transients are the primary acceleration sites. (2) We apply the Hillas criterion to relate this acceleration scale (L) to the maximum particle energy (E_{max}), a relationship validated through the presented Juno observations, previous research and recently shown to be applicable at planetary scales[5,34]. (3) We combine these scaling relations under the premise that foreshock transient-driven acceleration operates universally across collisionless shocks, independent of whether the system is a planetary bow shock, protostellar jet or supernova remnant. This final step represents an extrapolation beyond what is testable with in situ experimentation and relies on theoretical expectations regarding the physics of collisionless shocks in different astrophysical contexts, further discussed below. To model the maximum particle energies for the planetary systems shown in Fig. 3(b), we set the acceleration size (L) to the maximum observed value (L_{ext}). For the astrophysical objects, where direct observations of L are unavailable, we used our extreme fit model to estimate a value. Specifically, we calculated the upper boundary of the 95% prediction interval for a new observation at the object's system size (S). This interval accounts for both the uncertainty in the fitted model and the inherent variability in the data. The resulting energy range for each object, therefore, reflects the uncertainty propagated from its local shock speed and magnetic field parameters[66]. This approach provides an estimate for the maximum achievable energy that is constrained by direct observation for the planets and by a robust statistical extrapolation for the astrophysical shocks.

Physical justification for astrophysical applicability

The extension of the planetary-derived scaling to astrophysical environments necessarily involves an extrapolation beyond verifiable limits, as in situ measurements of foreshock localized processes at kiloparsec distances are not feasible for the foreseeable future. However, several physical arguments support this extrapolation as a reasonable theoretical expectation, grounded in our understanding of collisionless shock physics and the properties of astrophysical environments.

First, the astrophysical shocks that we consider (the protostellar jet HH 211 and the supernova remnants SN 1987A and SN 1006) represent curved, collisionless shocks, known from numerical simulations and indirect observational evidence to exhibit notable foreshock regions in their quasi-parallel geometries[2,8]. The curved geometry of these shocks ensures that quasi-parallel configurations are naturally present across substantial portions of the shock surface, similar to planetary bow shocks.

Second, although the predicted acceleration region scales of 10^8–10^{10} km for these astrophysical systems cannot be directly resolved, our estimates represent conservative lower bounds. These values are consistent with independent estimates of foreshock sizes[67,68]. The consistency between our extrapolated predictions and these observational constraints provides support for the validity of our scaling approach, even in the absence of direct spatial resolution of the acceleration regions themselves.

Third, the formation of large-scale foreshock transient can arise spontaneously through plasma instabilities and wave-particle interactions, whereas transient formation is also facilitated by large-scale discontinuities in the upstream medium[22]. These variable upstream media are an expected feature of astrophysical quasi-parallel shock environments. The turbulent interstellar medium contains magnetized filaments and structures extending to parsec scales[69–71]. Furthermore, supernova shock waves are expected to interact with complex

circumstellar structures created by the progenitor star itself. These include stellar wind-blown bubbles and previously ejected dense shells of material, which can extend to parsec scales[72–74]. When the expanding supernova shock encounters these pre-existing structures, it can generate large-scale magnetic field discontinuities. These encounters provide ideal conditions for seeding transient phenomena and driving particle acceleration through transient processes. Finally, the very high shock speeds observed at supernova remnants allow Alfvénic Mach numbers (M_A) to reach values of the order of 10^2–10^3, causing particularly strong foreshock regions upstream of their quasi-parallel geometries that are highly favourable for the formation and persistence of large-scale foreshock structures. We note, however, that the maximum extent of these structures may be regulated by the coherence length of the upstream magnetic field (L_B). For remnants in the galactic disk (for example, SN 1572), in which the shock radius can exceed L_B, the acceleration region might be affected by the coherence scale, possibly creating a plateau in the acceleration scale length. This is in contrast to high-latitude systems such as SN 1006 or young SRNs such as SN7D21987A, in which $L_B > S$. Overall, the interplay between tangled fields and foreshock development in the regime in which $S > L_B$ remains an open question for future investigation.

Although these arguments establish the physical plausibility of extending our planetary framework to astrophysical scales, we emphasize that this extrapolation remains tentative in the absence of direct observational confirmation. Nevertheless, the internal consistency of our framework, validated at planetary scales and yielding predictions for SN 1006 that match observed maximum energies of about 100 TeV, provides encouraging support for the underlying physical picture.

Parameters of Solar System planets

To apply our acceleration model, we first defined the physical parameter space for each environment. This space consists of the characteristic size (S), the acceleration region scale size (L), the shock speed (V_{sh}) and the upstream magnetic field strength (B) of the system. For the planetary environments, the system size S is the standoff distance of the bow shock, and L is the typical scale of a foreshock transient. These values were adopted from established literature[28,75], with the dataset for Jupiter supplemented by the event presented in this work. Minor refinements to the values have been made on the basis of the most recent standoff distance statistics and observations from each planetary environment[76–80]. A full range for the shock speed, V_{sh}, was selected for all environments to account for the variety of dynamic conditions observed at interplanetary shocks. This range is based on the typical relative speeds between the solar wind plasma and transient compressive structures, as documented in several previous works, with the upper limit essentially describing typical solar wind speed[4,5,28,81]. Finally, the range for the upstream magnetic field, B, at each planet was estimated using the Parker spiral model, which describes the evolution of the heliospheric magnetic field strength with increasing distance from the Sun[82].

Parameters for HH 211

HH 211 lies at approximately 1,000 light years away and drives a narrow bipolar jet with an associated bow shock. James Webb Space Telescope measurements showed speeds of about 80–100 km s^{-1} (figure 5 in ref. 7). Polarimetric ALMA/SMA observations have shown envelope magnetic fields of 40–100 μG (4–10 nT) within about 700 AU (refs. 83,84). The projected separation from the protostar to the bow shock is about 1,000 AU (figure 1 in ref. 7), which we take as the effective standoff distance. To account for variability, we took 700 AU as the system size (S), and a shock speed between 50 km s^{-1} and 150 km s^{-1} based on the observed outer shock. The relatively cold environment upstream of these propagating jets allows the local Alfvén Mach number (M_A) to be relatively high, subsequently causing the formation of a strong foreshock precursor.

Parameters of SN 1987A

SN 1987A in the Large Magellanic Cloud has been extensively monitored through radio and X-ray observations. During the interaction with the dense equatorial ring, the forward shock decelerated to around 2,300 km s^{-1}, later re-accelerating to 3,500–3,600 km s^{-1} (refs. 85–87); for our analysis, we used a conservative range between 2,000 km s^{-1} and 4,000 km s^{-1}. For the upstream interstellar magnetic field, we expect values of the order of 1–5 μG (0.1–0.5 nT)[88,89]. Finally, for an equivalence of a standoff distance of the expanding shock (or arc), we used the radius of the blast wave of 0.1 pc, resulting in an approximately 200,000 AU system size (S).

Parameters of SN 1006

SN 1006 is a young, shell-type supernova remnant that provides compelling evidence for efficient particle acceleration to very high energies, similar to other historical remnants, such as Tycho[90], Cas A[91] and RX J1713.7–3946[92]. Its shock velocity has been well-constrained by observations of its expansion, with estimates typically placing it in the range of 3,500–4,500 km s^{-1}. The strength of the upstream ambient magnetic field values is taken to be between 1 μG and 2 μG (0.1–0.2 nT). The system size of the remnant is approximately 9–10 parsecs, which translates to a system size (S) of roughly 2×10^6 AU. A unique feature of SN 1006 is the strong observational evidence, derived from its X-ray synchrotron and TeV emission, that particles are being accelerated to energies of the order of 100 TeV within its shocks[8,36,38]. This makes SN 1006 an ideal test case for evaluating acceleration frameworks and provides a direct benchmark for the predictions of our model.

The very high speeds observed at SN shocks allow Alfvénic Mach numbers (M_A) to reach values of the order of 10^3–10^4 causing a particularly strong foreshock upstream of their quasi-parallel geometry. This parameter range estimation is difficult to constrain as expanding SN shocks change during their lifetime. However, the parameter space above provides a reasonable order of magnitude estimate and uncertainty range for the maximum obtainable particle energy. The parameters for the planetary environments that were used for the fitting are shown in Extended Data Table 2, and all parameters used for our generalized maximum energy model are summarized in Extended Data Table 3. It should be noted that the obtained shock speed range for each planetary environment is predominantly driven by the relative speed of the solar wind with respect to the shock, whereas for astrophysical objects, it is primarily dictated by the outward shock expansion to the relatively stable interstellar medium. Finally, although the upstream magnetic field values used in this study may be elevated by compression effects within the foreshock or precursor region, the acceleration regions themselves are characterized by local magnetic depressions. Consequently, the magnetic field within these transient structures is expected to be notably weaker than in the surrounding environment.

Data availability

The JADE v.04 data from the Planetary Data System (PDS) data set JNO-J/SW-JAD-3-CALIBRATED-V1.0 (ref. 93) was used in this study. The calibrated spacecraft-corrected magnetic field vector measurements (MAG) used in this work were similarly obtained from the NASA Planetary Data System. JEDI data are also available from the Planetary Plasma Interactions Node of the Planetary Data System of NASA (https://pds-ppi.igpp.ucla.edu/collection/JNO-J-JED-2-EDR-V1.0). Requests for additional materials should be addressed to S.R.

Code availability

All figures were plotted using Python (v.3.12.5) and the matplotlib library (v.3.9.2). The version of the codes used, along with instructions on how to reproduce each figure and table, is accessible at

GitHub (https://github.com/SavvasRaptis/jupiter-bowshock-electron-acceleration[94]) or the associated Zenodo repository (https://doi.org/10.5281/zenodo.19582743).

47. Mauk, B. H. et al. The Jupiter Energetic Particle Detector Instrument (JEDI) investigation for the Juno mission. *Space Sci. Rev.* **213**, 289–346 (2017).
48. McComas, D. J. et al. The Jovian Auroral Distributions Experiment (JADE) on the Juno mission to Jupiter. *Space Sci. Rev.* **213**, 547–643 (2017).
49. Connerney, J. E. P. et al. The Juno Magnetic Field Investigation. *Space Sci. Rev.* **213**, 39–138 (2017).
50. Bagenal, F. et al. Magnetospheric science objectives of the Juno mission. *Space Sci. Rev.* **213**, 219–287 (2017).
51. Mauk, B. H. et al. Diverse electron and ion acceleration characteristics observed over Jupiter's main aurora. *Geophys. Res. Lett.* **45**, 1277–1285 (2018).
52. Wilson, R. J. Error analysis for numerical estimates of space plasma parameters. *Earth Space Sci.* **2**, 201–222 (2015).
53. Wilson, R. J. et al. Solar wind properties during Juno's approach to Jupiter: data analysis and resulting plasma properties utilizing a 1-D forward model. *J. Geophys. Res. Space Phys.* **123**, 2772–2786 (2018).
54. Kajdič, P. et al. Transient upstream mesoscale structures: drivers of solar-quiet space weather. *Front. Astron. Space Sci.* **11**, 1436916 (2024).
55. Kajdič, P., Blanco-Cano, X., Rojas-Castillo, D. & Omidi, N. Different transient phenomena at the edges of traveling foreshocks. *J. Geophys. Res. Space Phys.* **131**, e2025JA034777 (2026).
56. Joy, S. P. et al. Probabilistic models of the Jovian magnetopause and bow shock locations. *J. Geophys. Res. Space Phys.* **107**, SMP 17-1–SMP 17-17 (2002).
57. Karlsson, T., Raptis, S., Trollvik, H. & Nilsson, H. Classifying the magnetosheath behind the quasi-parallel and quasi-perpendicular bow shock by local measurements. *J. Geophys. Res. Space Phys.* **126**, e2021JA029269 (2021).
58. Koller, F., Raptis, S., Temmer, M. & Karlsson, T. The effect of fast solar wind on ion distribution downstream of Earth's bow shock. *Astrophys. J. Lett.* **964**, L5 (2024).
59. Svenningsson, I., Yordanova, E., Khotyaintsev, Y. V., André, M. & Cozzani, G. Classifying the magnetosheath using local measurements from MMS. *J. Geophys. Res. Space Phys.* **130**, e2024JA033272 (2025).
60. Balogh, A. & Treumann, R. A. *Physics of Collisionless Shocks: Space Plasma Shock Waves* (Springer, 2013).
61. Chu, C. et al. THEMIS satellite observations of hot flow anomalies at Earth's bow shock. *Ann. Geophys.* **35**, 443–451 (2017).
62. Turc, L. et al. Interplay between a foreshock bubble and a hot flow anomaly forming along the same rotational discontinuity. *Geophys. Res. Lett.* **52**, e2025GL116473 (2025).
63. Sonnerup, B. U. O. & Scheible, M. in *Analysis Methods for Multi-Spacecraft Data* (eds Paschmann, G. & Daly, P. W.) 185–220 (International Space Science Institute, 1998).
64. Davison, A. C. & Hinkley, D. V. *Bootstrap Methods and Their Application*. Cambridge Series in Statistical and Probabilistic Mathematics (Cambridge Univ. Press, 1997).
65. Haggerty, C. C. & Caprioli, D. dhybridr: a hybrid particle-in-cell code including relativistic ion dynamics. *Astrophys. J.* **887**, 165 (2019).
66. Heskes, T. Practical confidence and prediction intervals. In *Proc. Advances in Neural Information Processing Systems* Vol. 9 (NeurIPS, 1996).
67. Laming, J. M., Hwang, U., Ghavamian, P. & Rakowski, C. Electron heating, magnetic field amplification, and cosmic-ray precursor length at supernova remnant shocks. *Astrophys. J.* **790**, 11 (2014).
68. Katsuda, S. et al. Spatially resolved spectroscopy of a balmer-dominated shock in the cygnus loop: an extremely thin cosmic-ray precursor? *Astrophys. J. Lett.* **819**, L32 (2016).
69. Dickey, J. M. et al. Structure in the magnetic field of the Milky Way disk and halo traced by Faraday rotation. *Astrophys. J.* **940**, 75 (2022).
70. Ntormousi, E., Vlahos, L., Konstantinou, A. & Isliker, H. Strong turbulence and magnetic coherent structures in the interstellar medium. *Astron. Astrophys.* **691**, A149 (2024).
71. Beattie, J. R., Federrath, C., Klessen, R. S., Cielo, S. & Bhattacharjee, A. The spectrum of magnetized turbulence in the interstellar medium. *Nat. Astron.* **9**, 1195–1205 (2025).
72. Martizzi, D., Faucher-Giguère, C.-A. & Quataert, E. Supernova feedback in an inhomogeneous interstellar medium. *Mon. Not. R. Astron. Soc. Lett.* **450**, 504–522 (2015).
73. Moriya, T. J., Yoon, S.-C., Gräfener, G. & Blinnikov, S. I. Immediate dense circumstellar environment of supernova progenitors caused by wind acceleration: its effect on supernova light curves. *Mon. Not. R. Astron. Soc. Lett.* **469**, L108–L112 (2017).
74. Bykov, A. M., Ellison, D. C., Marcowith, A. & Osipov, S. M. Cosmic ray production in supernovae. *Space Sci. Rev.* **214**, 41 (2018).
75. Uritsky, V. M. et al. Active current sheets and candidate hot flow anomalies upstream of Mercury's bow shock. *J. Geophys. Res. Space Phys.* **119**, 853–876 (2014).
76. Winslow, R. M. et al. Mercury's magnetopause and bow shock from messenger magnetometer observations. *J. Geophys. Res. Space Phys.* **118**, 2213–2227 (2013).
77. Sulaiman, A. H., Masters, A. & Dougherty, M. K. Characterization of saturn's bow shock: magnetic field observations of quasi-perpendicular shocks. *J. Geophys. Res. Space Phys.* **121**, 4425–4434 (2016).
78. Gruesbeck, J. R. et al. The three-dimensional bow shock of Mars as observed by maven. *J. Geophys. Res. Space Phys.* **123**, 4542–4555 (2018).
79. Xu, S. et al. Closed magnetic topology in the Venusian magnetotail and ion escape at Venus. *Nat. Commun.* **15**, 6065 (2024).
80. Rutala, M. J. et al. New models of Jupiter's magnetopause and bow shock through the Juno prime mission: probabilistic location, shape, and internally-driven variation. *J. Geophys. Res. Space Phys.* **130**, e2025JA033842 (2025).
81. Turner, D. L. et al. Direct multipoint observations capturing the reformation of a supercritical fast magnetosonic shock. *Astrophys. J. Lett.* **911**, L31 (2021).
82. Owens, M. J. & Forsyth, R. J. The heliospheric magnetic field. *Living Rev. Sol. Phys.* **10**, 5 (2013).
83. Lee, C.-F. et al. Magnetic field structure in the flattened envelope and jet in the young protostellar system HH 211. *Astrophys. J. Lett.* **797**, L9 (2014).
84. Lee, C.-F. et al. Unveiling a magnetized jet from a low-mass protostar. *Nat. Commun.* **9**, 4636 (2018).
85. Manchester, R. N. et al. Imaging of the radio remnant of SN 1987A at 12 mm wavelength. *Astrophys. J.* **628**, L131 (2005).
86. Gaensler, B. M. et al. Fifteen years of high-resolution radio imaging of supernova 1987A. *AIP Conf. Proc.* **937**, 86–95 (2007).
87. Zanardo, G. et al. High-resolution radio observations of the remnant of SN 1987A at high frequencies. *Astrophys. J.* **767**, 98 (2013).
88. Berezhko, E. G. & Ksenofontov, L. T. Cosmic rays, radio and gamma-ray emission from the remnant of supernova 1987A. *Astron. Lett.* **26**, 639–656 (2000).
89. Berezhko, E. G. & Ksenofontov, L. T. Magnetic field in supernova remnant SN 1987A. *Astrophys. J. Lett.* **650**, L59–L62 (2006).
90. Morlino, G. & Caprioli, D. Strong evidence for hadron acceleration in Tycho's supernova remnant. *Astron. Astrophys.* **538**, A81 (2012).
91. Cao, Z. et al. Broadband γ-ray spectrum of supernova remnant Cassiopeia A. *Astrophys. J. Lett.* **982**, L33 (2025).
92. Aharonian, F. et al. A detailed spectral and morphological study of the gamma-ray supernova remnant RX J1713.7–3946 with HESS. *Astron. Astrophys.* **449**, 223–242 (2006).
93. Allegrini, F., Wilson, R. J., Ebert, R. W. & Loeffler, C. Juno J/SW Jovian auroral distribution calibrated V1.0, JNO-J/SW-JAD-3-CALIBRATED-V1.0 (NASA Planetary Data System, 2022).
94. Raptis, S. Jupiter-shock-acceleration: publish release. *Zenodo* https://doi.org/10.5281/zenodo.19582743 (2026).

Acknowledgements S.R. acknowledges funding from the Johns Hopkins University Applied Physics Laboratory independent R&D fund. S.R. acknowledges E. Batziou, F. Driessen, A. Lalti and M. Lindberg for their discussions. S.R. also acknowledges the International Space Sciences Institute (ISSI) team 465: 'Foreshocks Across the Heliosphere: System Specific or Universal Physical Processes?', team 555: 'Impact of Upstream Mesoscale Transients on the Near-Earth Environment' and the NSF GEM Focus Group 'Multiscale Dayside Transients and Their Effect on Earth's Magnetosphere'. D.L.T. acknowledges support from the NSF and NASA research grants (NSF grant no. 2225463 and NASA grant no. 80NSSC24K0173). D.C. acknowledges support from NSF AST-2510951. J.R.S. acknowledges NFDAP grant no. 80NSSC23K0665. Finally, we acknowledge the entire Juno team and the instrument principal investigators for data access and support.

Author contributions S.R. and D.L.T. conceptualized the study; S.R., D.L.T., D.C., G.C. and J.R.S. devised the methodology; S.R., D.L.T., D.C., G.C., C.C.H. and J.R.S. conducted the investigation; S.R., D.L.T. and J.R.S. visualized the study; S.R., D.L.T., D.C., G.C., C.C.H. and J.R.S. helped with funding acquisition; S.R. wrote the original draft; and S.R., D.L.T., D.C., G.C., C.C.H. and J.R.S. reviewed and edited the paper.

Competing interests The authors declare no competing interests.

Additional information

Supplementary information The online version contains supplementary material available at https://doi.org/10.1038/s41586-026-10473-z.

Correspondence and requests for materials should be addressed to Savvas Raptis.

Peer review information *Nature* thanks Philip Kirkeberg, Katariina Nykyri, Martin Pessah, Phil Valek and the other, anonymous, reviewer(s) for their contribution to the peer review of this work. Peer reviewer reports are available.

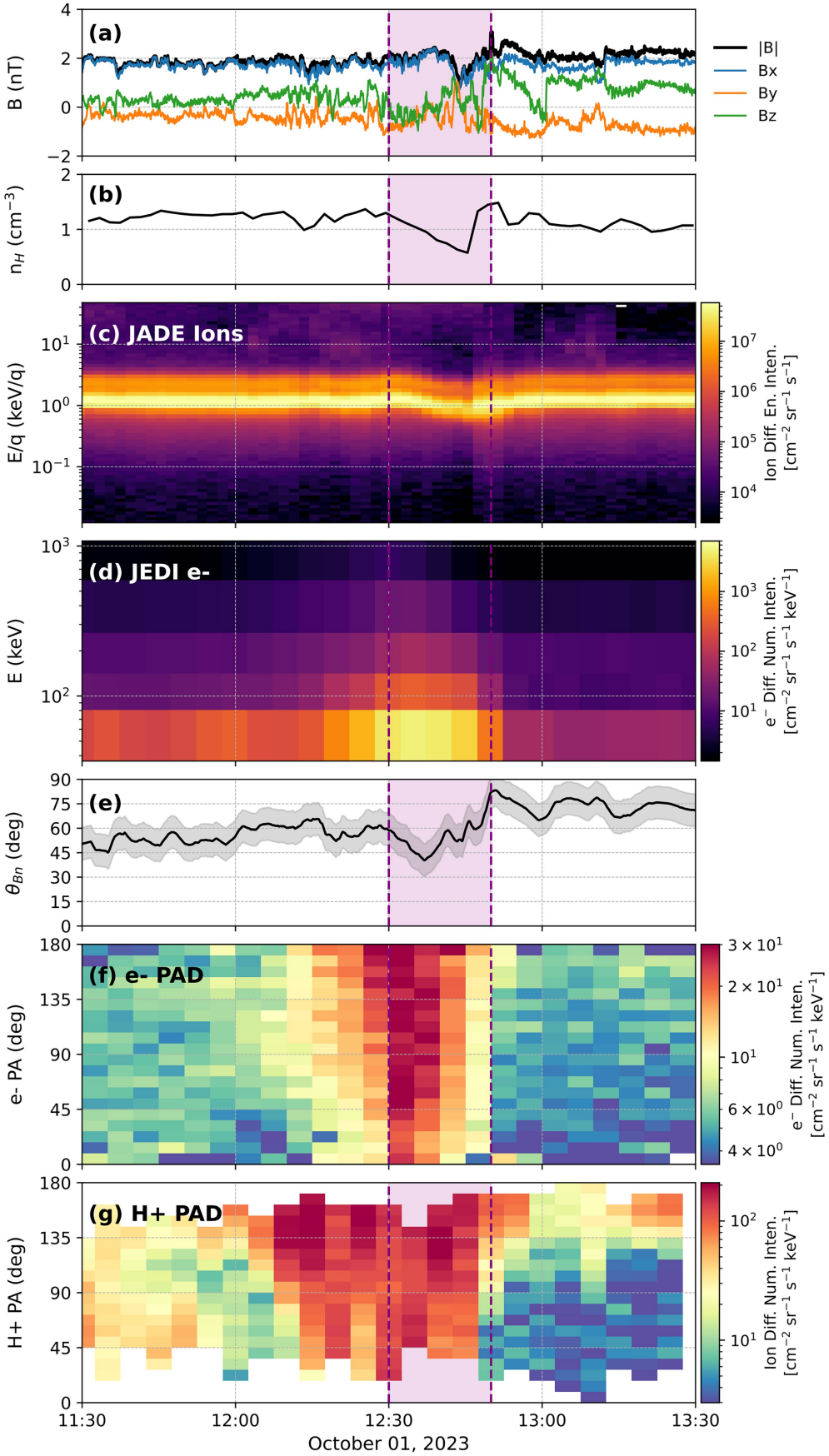

Extended Data Fig. 1 | See next page for caption.

Extended Data Fig. 1 | Detailed observations of the foreshock transient event. Detailed measurements are shown for the transient and the associated adjacent upstream region on October 1, 2023, between 11:30 and 13:30 UTC. (**a**) Magnetic field components and magnitude derived from the MAG instrument in nanotesla (nT). (**b**) Proton number density (n_H) derived from JADE in cm^{-3}. (**c**) Spectrogram of ion data from JADE in units of differential energy intensity. (**d**) Spectrogram of high-energy electron data from JEDI in differential flux units. (**e**) The angle between the magnetic field and the bow shock normal (θ_{Bn}), with associated uncertainty bounds of ± 5 degrees. **(f)** Energy-averaged electron pitch angle distribution from JEDI averaged between ~100 keV and 1 MeV energies. **(g)** Energy-averaged proton pitch angle distribution from JEDI averaged between ~30 keV and 1 MeV energies. The purple shaded region between 12:30 and 12:50 UTC highlights the main interval of the foreshock transient.

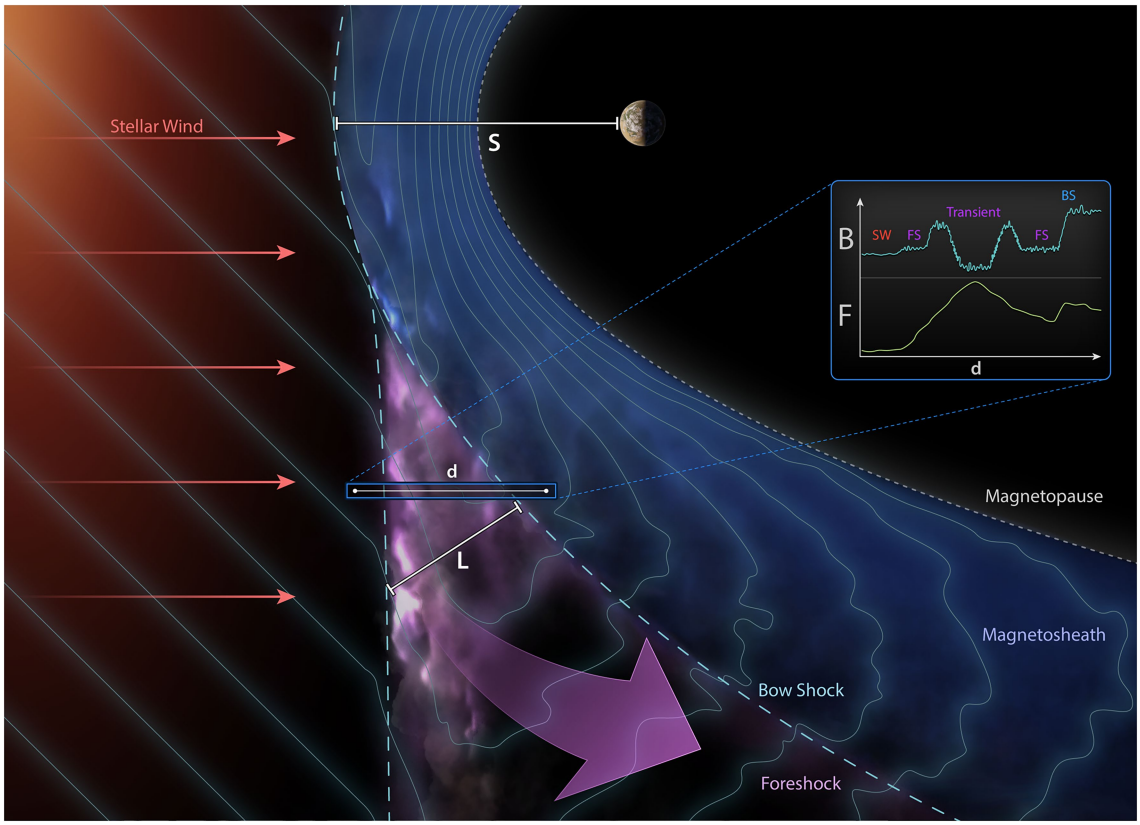

Extended Data Fig. 2 | Schematic representation of efficient particle acceleration within a foreshock transient. The illustration depicts the formation of a large-scale foreshock transient driven by a magnetic field discontinuity interacting with the planetary foreshock. The transient creates an extended region of turbulent interaction upstream of the main planetary bow shock. Note that for illustrative purposes, the transient scale length (L) is depicted as comparable to the global system scale (S), although as indicated by our analysis (See Fig. 3) for giant planetary magnetospheres (e.g., Jupiter), $S \gg L$. The inset displays a hypothetical spatial cut of observations transitioning from the unperturbed solar wind, through the foreshock and the transient structure, and finally crossing the planetary bow shock. Inset includes idealized observational profiles illustrate the evolution of the magnetic field ($|B|$) and energetic particle flux (F). The transient is characterized by a magnetic structure with a compressive edge and a depressed core, coincident with a localized burst of energetic particles. This peak flux in the upstream transient exceeds the intensities observed at the subsequent main bow shock crossing, illustrating the efficiency of the presented acceleration mechanism. Illustration by Ben C. Smith, Johns Hopkins Applied Physics Laboratory.

Extended Data Table 1 | Properties of the foreshock transient observed by Juno

Parameter	Symbol	Value
Interval Duration	Δt	≈ 900 s (15 min)
Solar Wind Speed (X-JSO)	$\mathbf{v}_{\mathrm{sw}}$	400 km/s
MVA Quality Ratio	$\lambda_{\mathrm{int}}/\lambda_{\mathrm{min}}$	5.82
Boundary Normal (JSO)	$\mathbf{n}_{\mathrm{MVA}}$	$[0.80, -0.58, 0.17]$
Effective Speed	v_{eff}	≈ 318 km/s
Transient Scale Size	L	2.86×10^5 km

Minimum Variance Analysis (MVA) was performed by combining data from periods bracketing the structure that correspond to a change in magnetic field direction. Specifically, the interval before the transient is taken as 12:30–12:40 UTC and after the transient as 13:02–13:10 UTC. v_{eff} describes the effective motion of the foreshock transient and is defined as $v_{\mathrm{eff}} = \mathbf{v}_{\mathrm{sw}} \cdot \mathbf{n}_{\mathrm{MVA}}$.

Extended Data Table 2 | Approximate scale sizes of foreshock transients

Planet	L_{typ} (km)	L_{ext} (km)
Mercury	1.5×10^3	1.0×10^4
Venus	4.0×10^3	1.0×10^4
Mars	1.0×10^4	4.0×10^4
Earth	1.5×10^4	1.0×10^5
Saturn	6.0×10^4	3.0×10^5
Jupiter	3.0×10^5	2.0×10^6

Foreshock transient scales at different planetary bow shock environments. Scale sizes *L* are based on typical and upper-bound values, expanded from the available literature[28,75].

Extended Data Table 3 | Parameter ranges used for obtaining the maximum particle energy range

Object	S (km)	$V_{\rm sh}$ (km s^{-1})	B (nT)
Mercury	5.0×10^3	[100, 600]	[10, 40]
Venus	8.0×10^3	[100, 600]	[5, 15]
Earth	1.0×10^5	[100, 600]	[3, 10]
Mars	1.0×10^4	[100, 600]	[1, 5]
Jupiter	6.0×10^6	[100, 600]	[0.5, 2.0]
Saturn	1.5×10^6	[100, 600]	[0.1, 1.5]
HH 211	$\sim 1.05 \times 10^{11}$	[50, 150]	[4, 10]
SN 1987A	$\sim 3.0 \times 10^{13}$	[2000, 4000]	[0.1, 0.5]
SN 1006	$\sim 3.0 \times 10^{14}$	[3500, 4500]	[0.1, 0.2]

Each astrophysical and planetary shock environment is associated with a system size (S), the shock velocity (V_{sh}) and the upstream magnetic field (B) from available literature (see associated subsection in Methods).